



Unraveling topography around subduction zones from laboratory models

Laurent Husson, Benjamin Guillaume, Francesca Funiciello, Claudio Faccenna

► To cite this version:

Laurent Husson, Benjamin Guillaume, Francesca Funiciello, Claudio Faccenna. Unraveling topography around subduction zones from laboratory models. *Tectonophysics*, 2012, 526-529, pp.5-15. 10.1016/j.tecto.2011.09.001 . insu-00676700

HAL Id: insu-00676700

<https://insu.hal.science/insu-00676700>

Submitted on 8 Mar 2012

HAL is a multi-disciplinary open access archive for the deposit and dissemination of scientific research documents, whether they are published or not. The documents may come from teaching and research institutions in France or abroad, or from public or private research centers.

L'archive ouverte pluridisciplinaire **HAL**, est destinée au dépôt et à la diffusion de documents scientifiques de niveau recherche, publiés ou non, émanant des établissements d'enseignement et de recherche français ou étrangers, des laboratoires publics ou privés.

Unravelling topography around subduction zones from laboratory models

Laurent Husson ^{*,a,b}, Benjamin Guillaume ^{c,d},
Francesca Funicello ^d and Claudio Faccenna ^d

^a*CNRS, Géosciences Rennes, Université de Rennes 1, Rennes, France*

^b*CNRS, LPG Nantes, Université de Nantes, Nantes, France*

^c*CNR-Istituto di Geologia Ambientale e Geoingegneria, Rome, Italy*

^d*Dipartimento di Scienze Geologiche, Università Roma Tre, Rome, Italy*

Abstract

The relief around subduction zones results from the interplay of dynamic processes that may locally exceed the (iso)static contributions. The viscous dissipation of the energy in and around subduction zones is capable of generating kilometer scale vertical movements at the surface. In order to evaluate dynamic topography in a self-consistent subduction system, we carried out a set of laboratory experiments, wherein the lithosphere and mantle are simulated by means of newtonian viscous materials, namely silicone putty and glucose syrup. Models are kept in their most simple form and are made of negative buoyancy plates, of variable width and thickness, freely plunging into the syrup. The surface of the model and the top of the slab are scanned in three dimensions. A forebulge systematically emerges from the bending of the viscous plate, adjacent to the trench. With a large wavelength, dynamic pressure offsets the foreside and backside of the slab by ~ 500 m on average. The suction, that accompanies the vertical descent of the slab depresses the surface on both sides. At a distance equal to the half-width of the slab, the topographic depression amounts to ~ 500 m on average and vanishes at a distance that equals the width of the slab. In order to explore the impact of slab rollback on the topography, the trailing edge of the plates is alternatively fixed to (*fixed* mode) and freed from (*free* mode) the end wall of the tank. Both the pressure and suction components of the topography are $\sim 30\%$ lower in the *free* mode, indicating that slab rollback

fosters the subsidence of upper plates. Our models are compatible with first order observations of the topography around the East Scotia, Tonga, Kermadec and Banda subduction zones.

Key words: subduction, dynamic topography, dynamic pressure, forebulge, analogue modeling

1 Introduction

The topography results from a variety of processes that, around subduction zones more than anywhere else, have strong spatial gradients. At the surface of the Earth, the conjunction of these processes not only produces the most important deviations from the geoid (outlined by the 5-10 km deep trenches), but also the largest topographic slopes, offshore and onshore. The topographic expression of subduction zones is viewed as the juxtaposition of a depressed bathymetry of the overriding plate, a deep trench, an outer rise (or forebulge). This structure correlates well with the gravity signal, in particular long wavelength geoid highs that correspond to the density anomalies of the subducted slabs, overprinted by sharp free air lows over the trenches that highlight the dynamic nature of the topographic depression, and an intermediate scale free air low that highlights the dynamic deflection of the overriding plate [1–5].

In fact, the processes that generate the total relief can be separated into the static components of the relief, that are primarily due to the lateral density variations within the lithosphere, and the more elusive dynamic topography that is, within its common geophysical sense, the response of the surface to the stresses that arise from the underlying mantle flow [6–9]. The process is presumably rather well known in theory, and a vast amount of work has focussed on explaining a variety of transgressive episodes thanks to models of dynamic topography around subduction zones [10–12, 5, 13–16]. However, the magnitude and wavelength remains highly uncertain (see e.g. Krien and Fleitout [17]). Indeed, even if many of the cited applications are appealing, Wheeler and White [18] conversely found no significant dynamic topography in South East Asia, where it is presumably represented at best, above the largest concentration of slabs at present-day. Uncertainty persists for several reasons.

First, the observation of the topography of the Earth around subduction zones is blurred by the convolution of complex mechanisms, and therefore requires meticulous analysis of, for instance, the admittance of topography and gravity

* laurent.husson@univ-rennes1.fr

31 signals [19]. But only a clear conception of the structure of the lithosphere
32 at a global scale, and at a degree that is almost always beyond our current
33 knowledge, could definitely solve this issue.

34 Second, confusion may arise from the definition of dynamic topography. In
35 fact, several components of the topography have a dynamic origin, and coining
36 it to the sole contribution of mantle flow underneath the lithosphere is not only
37 restrictive but misleading. In particular around subduction zones, a variety of
38 dynamic processes lead to the formation of, for the most obvious parts, the
39 forebulge and the trench.

40 Third, a variety of studies have individually explored the different mechanisms,
41 predicting a plausible relief that integrates all such processes is theoretically
42 rendered possible thanks to numerical models, even in three dimensions. How-
43 ever, at this stage, many technical challenges (free surface condition, three-
44 dimensional aspect) or mechanical issues (one-sided subductions, trench be-
45 havior, etc...) make numerical simulations around subduction zones neither
46 definitive nor consensual. In fact, only few attempts were done to capture all
47 the elements of the topography around subduction zones together [3,4,20,21].

48

49 Analogue models may offer an alternative. In this paper, we thus build upon
50 classic analogue models of subduction zones [22–24] to unravel the topography
51 around subduction zones. The following experiments therefore represent a first
52 attempt to model the topography around subduction zones self-consistently,
53 *i.e.* by examining the case of *free* subductions, wherein the dynamics is only
54 driven by the buoyancy of the slab and resisted by the viscous flow in the
55 surrounding mantle. Such setting is rendered possible thanks to the advantages
56 of laboratory models.

57 **2 The models**

58 *2.1 Experimental setup*

59 We carried out a set of 13 experiments that essentially reproduce the lines
60 of the experiments of [22] or [24] (Supplementary material 1). We use silicone
61 putty (Rhodrosil Gomme, PDMS + iron fillers) and glucose syrup to model the
62 lithosphere and the upper mantle, respectively. Silicone putty is a viscoelastic
63 material but its Maxwell time (< 1 s) precludes any elastic behavior in our
64 models lasting several minutes. Glucose syrup is a transparent Newtonian low-
65 viscosity and high-density fluid. These materials have been selected to achieve
66 the standard scaling procedure for stresses scaled down for length, density and

viscosity in a natural gravity field as described by Weijermars and Schmeling [25] and Davy and Cobbold [26].

The scale factor for length is 1.5×10^{-7} (1 cm in the experiment corresponds to 66 km in nature) (Table 1). Densities and viscosities are assumed to be uniform over the thickness of the individual layers and are considered to be averages of the actual values. For the reference model, described hereafter, the negative buoyancy of the lithosphere is -91 kg/m^3 (Table 1). The viscosity ratio between the slab and the surrounding mantle (η_l/η_m) is 1.4×10^4 . This value appears to be an upper bound according to recent studies [21,27–30].

2.2 Experimental procedure

The system is disposed in a 80 cm wide square tank (fig. 1). The experimental subduction is always initiated by artificially forcing the leading edge of the silicone plate into the glucose downward to a depth of 3 cm (corresponding to about 200 km in nature). We complemented the standard setup [22] by adding a laser scan (**put the reference of the old laser? I don't have them**) above the tank and digitize the deforming topography. The laser is capable of acquiring the topography with a maximum horizontal resolution of 0.13 mm. The precision of punctual topographic data is 0.05 mm (**this is for new laser**), which considerably improves when a statistical treatment is applied. In the following, we refer to the side of the unsubducted portions of the plate as the foreside and conversely, the backside is the region above the sunken slab (fig. 1).

For modeling conveniency, each experiment is separated into two sub-experiments. The first stage of the experiments takes place within the framework of *fixed edge* subduction *sensu* Kincaid and Olson [31], *i.e.* the trailing edge of the slab is attached to the tank in order to preclude any trenchward motion of the silicone plate. When steady state is reached (when the generic *S* shape of the retreating slab is reached and the geometry remains unchanged in the referential of the moving trench), the shape of the silicone slab is scanned before the surface is spray-painted (in order to overcome optical issues due to the translucency of the glucose syrup) and scanned as well. When all measurements are done, the trailing edge of the silicone slab is freed from the tank, and the subduction enters a *free edge* mode for a second sub-experiment. Because the surface remains painted from the first stage, it is technically impossible to scan the surface of the slab at depth without strongly damaging the experiment. Only the topography of the surface of the model is thus acquired when a new steady state is reached.

Our simplified subduction system is designed in order to impose a straightforward force balance that approximately reproduces that of plate tectonics: the slab drives the flow in the glucose syrup and is resisted by the viscous dissipation in the glucose syrup and slab. It simply reads $F_{sp} + F_{rp} = F_v + F_b$, where F_{sp} is the slab pull force, with $F_{sp} = (\rho_l - \rho_m)gWz_s\frac{H}{\sin\alpha}$, where g is the gravitational acceleration, H and W the thickness and width of the slab, z_s the depth of the leading edge of the slab ($z_s = D$ in steady state, where D is the thickness of the glucose syrup layer), and α the dip of the slab. $F_{rp} = (\rho_l - \rho_m)g\frac{H^2}{2}$ is the ridge push force, which in the *free* mode is negligible with respect to the slab pull force [22]. In the *fixed* subduction mode, the situation differs because of the no motion boundary condition. This kinematic (as opposed to dynamic) condition implies that F_{rp} constantly adjusts to balance the trenchward force that applies to the plate. That force is the opposite of the integral of the trench perpendicular component of the horizontal shear stresses underneath the lithosphere. These stresses result from the underlying viscous flow in the syrup, ultimately excited by the subduction of the slab. Paradoxically in that mode, the sign of F_{rp} implies that, as opposed to the situation on Earth, it is a resisting force.

F_b is the bending force of the silicone slab. Funiciello et al. [27] computed the total value of F_b by integrating its local values along the bent lithosphere, such that $F_b = \int_i \frac{2}{3}W\eta_l v_{sub}(H_i/r_i)^3 di$, where H_i is the varying thickness of the slab alongside the slab length and r_i is the varying radius of curvature. η_l is the dynamic viscosity of the silicone putty and v_{sub} is the subduction velocity. The viscous dissipation due to slab bending in our models (10 to 30% [27]) is possibly slightly overestimated compared to that of the Earth. First, it is counted twice because the plate bends at the surface, but also at the bottom of the tank, where the slab retrieves a flat, horizontal geometry. In addition, because our slab to mantle viscosity ratios, when scaled to the Earth, are in the high end of the inferred range of values [27,32,30], the bending force may be high. In real Earth, it is now thought that the bending dissipates less than $\sim 25\%$ of the energy [29], and even more likely between 5 and 20% [33].

Last, the viscous force F_v that stirs the glucose syrup is more difficult to assess; there is no proper analytical solution besides scaling F_v with $\eta_m v$ (where v is the rate at which the slab rolls back). Indeed, this is particularly unfortunate because that viscous flow is responsible for the long wavelength dynamic distortion of the surface.

142 Before going further, a few limitations that are intrinsic to our models should
 143 be outlined. First of all, the seldom discussed surface tension [34,35] affects
 144 the dynamics of our experiments. In a sense, surface tension can conversely
 145 be regarded as fortunate, because it coincidentally holds at the surface the
 146 silicone plates, whose buoyancies fall within the desired range of exploration,
 147 and let them sink beyond. However this is not an Earth-like property and
 148 as such it may alter the interpretation of subduction dynamics. In addition,
 149 the paint layer may also modify the surface tension of the fluid with respect
 150 to the experiments that are exempt of paint. The effect of surface tension is
 151 critical only when the slab buoyancy forces are low enough to be comparable
 152 to that of surface tension. It could explain the non-linear behaviour of some
 153 analogue models. For instance, in the experiments of Schellart [23], subduction
 154 kinematics do not scale linearly with slab buoyancy, that is presumably the
 155 only varying parameter of the experimental serie. However, such non linearities
 156 are not striking in the experiments of Funiciello et al. [22]: during the early
 157 stages of subduction, trench retreat rates seemingly increase almost linearly
 158 with the slab pull force. Therefore, we assume that the role of surface tension,
 159 although non negligible [35], doesn't significantly bias our results, but should
 160 be carefully considered when full parametric studies are carried out.

161 Second, our models have no overriding plates. In precursory models, [36] suc-
 162 cessfully overcame this issue by adding a viscous upper plate and measuring
 163 the elevation changes throughout the experiment. This was suited for their
 164 applied experiments, but added some noise to the results. Here instead, as in
 165 the seminal experiments of subduction zones [22–24], we simplify the models
 166 in order to extract the quintessential processes that shape the surface of the
 167 Earth around subduction zones, but also to evaluate the feasibility of such
 168 technique from a general standpoint. We are well aware that introducing up-
 169 per plate changes the subduction dynamics [17,37,38], but a full parametric
 170 study, that would explore a variety of boundary conditions (including upper
 171 plates) is beyond the scope of this paper.

172 Third, the tank is not infinite, which often appears satisfying enough for the
 173 study of subduction dynamics in general [22–24]. However, given that the very
 174 distribution of the stresses within the flowing glucose syrup controls the to-
 175 pography, its perturbation by the non-infinity of the tank plays a role. This
 176 imposed condition nevertheless partly compares to real Earth, wherein slabs
 177 neither sink into an infinite mantle nor evolve within a domain bounded by
 178 undeformable, finite boundaries. This intermediate situation is often mislead-
 179 ing when comparing real Earth subduction dynamics to simplified models that
 180 display framed isolated systems.

181 3 Results

182 All our models follow comparable evolutions. Once steady state is reached, the
 183 slab is folded twice, at the surface and at the bottom of the tank, where it lit-
 184 erally unfolds. Subduction freely occurs: it is driven by the sole slab buoyancy
 185 and resisted by the viscous flow in the glucose syrup. The slab enters a classic
 186 rollback subduction mode. The trench therefore retreats while the slab sweeps
 187 back into the glucose syrup, which in turn is displaced from the foreside to
 188 the backside of the model thanks to a combination of toroidal and poloidal
 189 flows [39,40,28] (fig. 2). When it enters the *free* subduction mode, the plate
 190 moves trenchward, therefore reducing the rates of slab rollback ($\sim 12\%$ for
 191 model 1 for instance). The slab consequently becomes steeper. The dynamics
 192 of subduction, *i.e.* the motion of the slab and the viscous flow in the glucose
 193 syrup, excited by the very motion of the slab, alter the static force balance
 194 and reshape the surface of the Earth. Our models allow to unravel the various
 195 components.

196 3.1 *Departure from isostasy as an indicator of the force balance in the system*

197 The depth h of the silicone layer relative to the glucose syrup is in principle,
 198 in isotatic conditions, determined by the buoyancy of the layer, such that $h =$
 199 $\int_H \frac{\rho_l - \rho_m}{\rho_m} dz$, where ρ_m and ρ_l are the densities of the glucose syrup and of the
 200 silicone putty, H being the thickness of the silicone layer. Indeed, unsubducted
 201 portions of the slab lay at greater depths than the adjacent glucose syrup. This
 202 component dominates at the large scale and explains the first order observation
 203 of the topography (figs. 2, 3 and 4). (Note that, unlike the Earth's lithosphere,
 204 the silicone layer is not bounded by neighboring plates and therefore elevation
 205 decreases stepwise from the adjacent glucose syrup. This discontinuity would
 206 cause the silicone plate to subduct if surface tension was not high enough
 207 to prevent this from happening, as illustrated by the meniscuses that make
 208 the transition from the elevation of the glucose syrup to that of the silicone
 209 plate, fig. 4b). Note that this it is not surface tension that plays this role on
 210 Earth but the fact that oceanic plates are not in isolation from one another.
 211 It is simply the lateral continuity of the lithospheres that prevents the lighter
 212 underlying mantle from welling above the plates.

213 A closer examination of the topography reveals that it departs from isostasy
 214 at different spatial scales, that are due to the dynamic evolution of the system.
 215 The viscous dissipation of the energy modifies the static equilibrium. It bends
 216 the silicone plate, which produces some relief, and stirs the glucose syrup,
 217 which also deforms the surface. In the glucose syrup, the viscous dissipation
 218 can be separated into the poloidal (in the vertical plane) and toroidal (in

the horizontal plane) components. The retrograde motion of the slab into the syrup modifies the horizontal stress field and its descent into the fluid induces the vertical one. The convolution of these dynamic processes causes, across subduction zones on Earth, a variety of features that can be deciphered thanks to our integrative experiments.

3.2 Trench

The most obvious feature that departs from the static topography is naturally the trench (figs. 3, 4 and 5). Trench depths reach ~ 3 -4 mm and do not vary significantly from the *fixed* mode subduction mode to the *free* mode (fig. 4a). Along-strike (parallel to the trench), the trench is almost uniformly deep; only at very short distances (less than a fifth of the slab width) from the slab edges does it shallow (fig. 3); this highlights that this structure is essentially two-dimensional, across strike. In real Earth, the depth of the trench is determined by the shear coupling between the upper and lower plates on the interplate fault [4,41]. Our model is purely viscous and there is therefore no proper subduction fault that could be defined by a yield stress. Instead, the depression results from the competition between the buoyancy stresses in the glucose syrup, that tend to restore uniformity, and the shear stresses exerted by the subducting slab that impose the downward flow of the glucose syrup. The main difference is that the flow in the wedge has a boundary condition that is more kinematic, imposed by the subduction rate, than dynamic, *i.e.* defined by a shear stress. The glucose syrup at the interface therefore must flow along with the subducting plate. Note that part of the apparent trench in our models is a meniscus from surface tension (see above). Scaled to the Earth, predicted trench depths amount to 20-25 km, which seems impressively unrealistic, but is in fact only approximately two to three times larger than actual trenches (after sediments are stripped off).

3.3 Viscous bulge

Adjacent to the trench is the forebulge on the silicone plate (figs. 3, 4 and 5). Bulges in our experiments result from the viscous flexure of the silicone plate. Their 0.15 to 0.2 mm high, 75 ± 25 mm wide, elongate bodies lie parallel to the trench, at a distance that varies of ~ 50 mm in the *free* mode and ~ 44 mm in the *fixed* mode. This difference arises from the fact that slabs are steeper in the *free* mode, a fact that doesn't affect the elevation of the bulge that remains comparable in both cases. This may be explained by the fact that subduction rates play a fundamental role. Indeed, if the rate of trench retreat is lower of 12% in the *free* mode, the subduction rate remains comparable.

Contrarily to the trench, the bulge reaches its maximum elevation near the edges of the plate, and not in the center (figs. 3 and 5). This observation is somewhat surprising given the fact that the flexure of a viscous plate is *a priori* a two-dimensional problem and as such, there is no intrinsic reason for the bulge to have its elevation vary along-strike. It results from the interaction with the suction component, which is larger in the center of the slab than at the edges (see section 3.5).

In theory, the viscous flexure of the plate is periodic, and the magnitude of the oscillation diminishes exponentially towards the foreside [42,43]. The forebulge should therefore be followed by a deflection, but its magnitude is too small to be detected in our experiment. Not surprisingly, the plate flexure follows the universal deflection profile [42]. Scaled to the Earth, the modeled bulges are 1.0 to 1.3 km high and 500 ± 175 km large. The distance between the maximum elevation of the bulge and the trench varies from ~ 335 km to ~ 300 km, depending on the mode. Our models here reemphasize the possibility that the observed outer rises are due to the viscous nature of the lithosphere [43,41].

3.4 Overpressure

The depth of the silicone plate is systematically offset by $\sim 100 \mu m$, with respect to the theoretical, isostatic depth, when the subduction occurs in a *fixed* mode, and is 30% smaller on average in the *free* subduction mode (fig. 4a). This is a first order response of the topography to the underlying force balance, in the glucose syrup. The retrograde motion of the slab compresses the glucose syrup in the foreside and conversely, extends it in the backside. The situation is somewhat similar to that of a channel flow between the slab itself and the end wall of the tank, such that $\frac{dp}{dy} = 12\eta_m \frac{\bar{v}}{L^2}$, where $\frac{dp}{dy}$ is the pressure gradient in the channel parallel to the slab, η_m is the dynamic viscosity of the glucose syrup, \bar{v} is the mean velocity in the channel, and L is the width of the channel. Mass conservation imposes that $\bar{v}L = u\frac{W}{2}$, where u is the horizontal velocity of the slab and $\frac{W}{2}$ is the half width of the slab. The mean pressure in the channel is $\bar{p} = \frac{3}{2}\eta_m \frac{uW^2}{L^3}$. That dynamic pressure is compensated by a mean deflection of the surface that reads

$$\bar{\delta}_z = \frac{3\eta_m}{2\rho_m g} \frac{uW^2}{L^3}. \quad (1)$$

u is counted negative on the backside and positive on the foreside, therefore the two effects amplify the total elevation offset between the front and back of the slab, which therefore approximately equals $2\bar{\delta}_z$ (if the slab plunges into the syrup at an equal distance from each end of the tank). It gives a order of magnitude for $2\bar{\delta}_z$ of 5 to $100 \mu m$ depending on the experimental values. The

293 scaled magnitude of the offset is thus 35 to 700 m, depending on the forces
 294 at play and on the subduction mode. These results are in the lower bound
 295 of our observations which reveals that this approximation may not be robust
 296 enough to be further developed. In particular, because the finite geometry of
 297 the tank in which the channel is embedded is not accounted for, the channel
 298 flow analogy does not permit to explain the uplifted topography outside the
 299 channel proper, on the glucose syrup adjacent to the slab. It is nevertheless
 300 obviously related to the same overpressure induced by the retrograde motion
 301 of the slab (fig. 1). Indeed in our models, the overpressure effect occupies the
 302 entire surface of the tank. It induces an overall tilt of the surface and is not
 303 restricted to the surface of the plate. This figure only partly compares to real
 304 Earth where plates do not subduct in bounded domains (but neither sink in
 305 an infinite mantle).

306 Because in the *free* subduction mode, part of the pressure is released when
 307 the slab is free to move trenchward (*free subduction*), the elevation offset is
 308 lower than the offset in the *fixed* mode (trench migration rates, and therefore
 309 pressure, are lower); it then amounts to ~ 500 m on average. This can per-
 310 haps be more clearly conceived by stating this in a more rigorous way, that
 311 reverses causes and consequences: the very reason why trenches roll back at
 312 lower rates in the *free* subduction mode than in the *fixed* mode is indeed the
 313 pressure drop between the fore and backsides of the slab. Overpressure on the
 314 foreside, underpressure on the backside partly work to maintain the slab at a
 315 central location in the tank. In the particular case where the pressure gradient
 316 balances the slab normal component of the slab pull force, no roll back occurs
 317 [20]; this situation is never met in our models.

318 3.5 Suction

319 At second glance, second order deflections burst out: the topography shows
 320 a large scale deflection centered on the trench (figs. 2 and 3), the wavelength
 321 of which is much larger than that of the trench. This is the dynamic re-
 322 sponse of the topography to the vertical motion of the slab, a largely debated
 323 feature on Earth's subduction zones [3–5,44,18,45]. It is often referred to as
 324 *dynamic topography*, despite the fact that the other topographic features, be-
 325 sides isostasy, are also *dynamic* in essence. The descent of the slab induces
 326 stresses that are compensated by a vertical deflection of the topography δ_z ,
 327 so that $\delta_z = \sigma_{zz}/\rho_m g$, where σ_{zz} is the vertical stress due to the poloidal flow
 328 in the glucose syrup. It forms a depression that is visible in both the foreside
 329 and backside of the trench (figs 3 and 4). In the *fixed* subduction mode, the
 330 measured magnitude of the deflection in our experiments is around 75 ± 50
 331 μm at a distance $W/2$ (half width of the slab) from the trench, depending on
 332 the forces in the presence and setting. This corresponds to 500 ± 330 m when

333 scaled to the Earth. The deflection reaches its largest magnitude in the center,
 334 above the slab, and vanishes laterally, both along- and across-strike. The lat-
 335 eral extent of the anomaly is theoretically infinite in a linear viscous flow but
 336 visual inspection of our experiments reveal that the magnitude of the dynamic
 337 deflection becomes negligible at an approximate distance W from the trench.
 338 On the foreside, the dynamic deflection combines with the short-wavelength,
 339 large-magnitude features that are the trench itself and the forebulge (fig. 5).
 340 Note that it shall not be confused with the secondary harmonic oscillation
 341 of the viscous flexure, because the magnitude is incompatible. Typically, the
 342 universal deflection curve for a viscous bulging gives a ratio between the mag-
 343 nitudes of the forebulge and of the depression that follows of about 1/100 [43]
 344 after [42], which is considerably less than the 20 to 30% given by the ratio
 345 between the elevation of the forebulge and the deflection.

346 *Free* subduction mode (fig. 3b) also naturally produces suction, but *fixed* sub-
 347 duction systems display wider and deeper dynamic deflections than *free* mode
 348 ones by about 30%. The shape of the deflection relates to the distribution of
 349 the mass anomalies at depth and therefore to the shape of the slab in our
 350 experiments. Because in the *free* subduction mode, slabs are steeper [22], the
 351 mass excess lays, on a map view, closer to the trench. This makes the wave-
 352 length of the dynamic deflection shorter. In addition, in the *free* subduction
 353 mode, the total mass is smaller because the slab is steeper, and therefore
 354 shorter (total mass varies like $D \sin \alpha$, where α is the slab dip angle). In our
 355 experiments, slab dip increases from $\sim 60^\circ$ to $\sim 80^\circ$ between the *fixed* and
 356 *free* modes (Ben, can you put in the correct values?). This decreases the
 357 total mass anomaly by $\sim 15\%$, the slab pull by a similar amount and, if the
 358 geometry remained the same, the magnitude of the dynamic deflection too.
 359 Because the shape of the slab also changes in the experiment, the modification
 360 is not linear, and the deflection in the *free* mode is also sharper.

361 Dynamic deflections are time-dependent and the successive scans that we per-
 362 formed during the transition from a *fixed* subduction mode to a *free* subduc-
 363 tion mode are also available. Similarly, we performed some experiments during
 364 which the buoyancy of the slab that enters the subduction varies. This also
 365 induces transient behaviors. Typically, the slab is made up of a succession of
 366 segments of low and high buoyancies (models 12 and 13, see parameters in
 367 Supplementary material 1). We monitored the transient topographic response
 368 to the dynamics of subduction through time. As expected, low buoyancy seg-
 369 ments are accompanied by smaller dynamic deflections than high buoyancy
 370 ones, and reciprocally. These transient regimes shall be compared to the geo-
 371 logical record around subduction zones. But this step shall not be envisioned
 372 before steady regimes are understood and identified on Earth.

373 4 Comparison to the figure of the Earth

374 Our simple setup resembles the Earth to some extent. It therefore permits to
 375 quantify the relative importance of each of the contributors that shape the
 376 figure of the Earth around subduction zones. In fact, a variety of models was
 377 formerly designed at the scale of the subduction zone in order to explore the
 378 relationships between the slab and dynamic topography. Few of them how-
 379 ever challenge the technical issue of incorporating mobile trenches, although
 380 it is known to affect the response of the surface topography [20]. Because
 381 they generally aim at quantifying dynamic topography of the overriding plate
 382 and neglect the subducting plate, most models implicitly ignore the fact that
 383 they constantly modify artificially the stress balance in order to maintain a
 384 no rollback condition. The consequences of this choice are not trivial : trench
 385 motion controls the flow around subduction zones -and therefore the stress
 386 regime- to a degree that may have a profound impact on the flow pattern in
 387 the wedge [46]. Imposing trench fixity barely resembles Earth-like conditions
 388 and in our models, we adopt two alternative settings. The *fixed* mode con-
 389 sideres that the stresses that resist the displacement of the subducting plate
 390 are always large enough to oppose any motion. In that case, trench migration
 391 rates equal subduction rates. This example is relevant to the Earth in many
 392 instances. For instance, the small-scale subduction zones that are embedded
 393 into bigger systems (like the fast Hellenic subduction zone within the slow
 394 Africa-Eurasia convergent system, or the East Scotia subduction zone within
 395 the South Atlantic). The *free* subduction mode instead assumes that plate
 396 motion is dictated by the force balance at the subduction zone itself. This
 397 mode could correspond to any larger subduction system (for instance, Nazca-
 398 South America) under the heavy assumption that the upper plate doesn't play
 399 a crucial role in the force balance. In our experiments, *fixed* subduction sys-
 400 tems display wider and deeper dynamic deflections than *free* mode ones. Such
 401 result is beyond what could be inferred by a comparison between the Nazca
 402 and Hellenic subduction zones; in that sense, analogue models are helpful to
 403 overcome observational issues.

404 The forebulge is a commonly described feature and it is no surprise that it is
 405 well reproduced by our models. As opposed to the more popular elastic bulge
 406 [2,42,47], our models predict that outer rises emerge from the flexure of viscous
 407 slabs. This idea is however not new: similar geometries have been reproduced
 408 with either viscous or elastic rheologies [43], or even with composite rheologies
 409 [48,49]. However, given the fact that subducting slabs are dominantly treated
 410 with viscous rheologies in the litterature, it is good to recall that outer rises
 411 may be caused by a process that consistently obeys the same rules. Our models,
 412 as many others, is capable of predicting the variable geometry of outer rises
 413 to a degree that exceeds observations. In fact, flexure models became popular
 414 although they mostly apply to the Aleutian, Kuril, Bonin, and Mariana, *i.e.*

a selection of well-behaved subduction zones that were chosen as early as the 70's to illustrate the theory [2]. Herein we wish to emphasize that, more than the forebulge, that almost only depends on the rheology of the subducting plate, or even the trench, it is the surface expression of the underlying viscous flow that those experiments reveal with a new light.

Interestingly enough, the suction deflection appears on both the back and fore sides of the trench. Global models that are buoyancy driven [7–9,16] also show this, because slabs are the prominent features in the Earth's mantle. But again, models that are designed to investigate the relationships between the subducting slab and the dynamic deflection of the upper plate do not consider the dynamic topography on subducting plates but only focus on upper plates. Our models show that subducting plates (foreside of our models) can also be deflected downward by the suction effect of the underlying mantle flow, by a comparable amount. The signal is not straightforward though, because although it is of opposed sign, this depression competes with the uplift due to the overpressure underneath the foreside of the slab. Therefore, the net result is a global uplift of the foreside, only modulated by the shorter wavelength suction topography (fig. 5). The overpressure effect is expected to uplift the subducting plate at a regional scale by 100 to 600 m. Only at short distance from the trench, this effect should be counterbalanced by the opposite effect of the suction.

In real Earth, the signal is often too blurred to detect the competition between the two processes. It is nevertheless true that the bathymetry, to the East of the East Scotia subduction zone is ~ 5000 m deep (fig. 6a), almost 1000 m deeper than the surrounding portions of the Atlantic plate of similar age. The Tonga and Kermadec subduction zones (considered as two different subduction zones separated by a slab tear from one another at the junction with the Louisville ridge) display comparable relief: the seafloor to the East of the Tonga trench (fig. 6b) lies at ~ 6000 m, and to the East of the Kermadec trench at 5800 m (fig. 6b). In all three cases, the seafloor lies 500 to 1000 m lower (avoiding seamounts) than the surrounding portions of the oceanic plate of similar age. The distance at which the depression becomes insignificant is comparable to the width of the trench, which is remarkably corroborating the suction effect observed in our experiments. In addition, these depressed areas are possibly embedded in wider zones that are themselves possibly at higher elevations than more distal portions of seafloor of similar age. The ages of the foresides of the East Scotia Sea is 30 to 50 Ma, that of Tonga is 90 to 100 Ma, and that of Kermadec is 90 to 120 Ma. The expected depth, compared to the mean depths on Earth [50] are respectively 4800 ± 400 m, 5400 ± 400 m, and 5500 ± 400 m. The seafloor, in all three cases is 200 to 600 m shallower than the mean values for the Earth, which is in turn comparable to the prediction of the overpressure effect from our experiments (the observed offset is

458 $\bar{\delta}_z$, not $2\bar{\delta}_z$ because only the overpressure on the foreside is measured). Last,
 459 the inferred suction effect in the Tonga subduction zone is more pronounced,
 460 by ~ 200 m, than in the adjacent Kermadec subduction zone. The subducting
 461 plate in the Tonga and Kermadec subduction zones is presumably comparable
 462 for it has the same nature. The only *a priori* differences between the two are
 463 (i) a slightly older subducting slab in the South (Kermadec) than in the North
 464 (Tonga), which should *a contrario* enhance the suction effect because of the
 465 higher negative buoyancy, and (ii) a much faster slab rollback in the North
 466 than in the South. The latter effect efficiently shapes the bathymetry: while
 467 the Kermadec trench remains approximately stationary, the Tonga trench is
 468 the fastest retreating trench on Earth, at about 160 mm/yr. This observation
 469 supports our model results, which suggest that rollback fosters dynamic to-
 470 pography: dynamic deflections of the topography in the *free* subduction mode
 471 are lower by $\sim 30\%$ than in the *fixed* mode. Similar conclusions were reached
 472 by Russo and Silver [51], who envisioned the possibility that the shallow Nazca
 473 plate could be uplifted by the underlying dynamic overpressure. These obser-
 474 vations certainly plead for the existence of dynamic deflection of the foreside
 475 of the subduction zones too, but making the link between the two requires a
 476 thorough analysis of the bathymetry and gravity.

477 On the backside however, the effects of dynamic pressure and suction have the
 478 same polarity; the cumulated depression predicted by our models thus amounts
 479 to 1200 ± 500 m. At large distances from the trench, only the underpressure
 480 effect remains significant, with a downlift of 100 to 600 m. Many examples in
 481 continental domains [12–15, 36, 52, 53] display geological signatures that confirm
 482 that upper plates are deflected by comparable magnitudes and wavelengths.
 483 The long wavelengths of the afore cited examples highlight the importance
 484 of the underpressure effect in continental inundation more than that of the
 485 suction effect.

486 In oceanic domains, the underpressure effect on the backside is more difficult
 487 to track on Earth because few subduction zones display clear enough settings.
 488 The few candidates are the Philippine plate (40–50 Ma) and the South Fidji
 489 basin (20–30 Ma), that respectively lay at ~ 5900 m and ~ 4500 m. Their depths
 490 are thus respectively ~ 1000 m and ~ 300 m deeper than the mean average
 491 depth for seafloor of similar ages [50], which again pleads for a deflection
 492 that is at least compatible with our model results. The suction effect on the
 493 backside is more clearly expressed in oceanic domains. At short distances from
 494 its trench, the 8000 m deep Weber trough in the Banda Sea (fig. 7a) represents,
 495 in spite of its extremely young age (< 3 Myrs), the deepest seafloor on Earth
 496 besides trenches at present-day. It is more than 5000 m deeper than the mean
 497 depth of oceanic units of similar age. Similarly, the residual topography of the
 498 East Scotia sea back arc basin (fig. 7, modified after [5]) is deflected towards
 499 its center by up to 1500 m at a short distance from the trench. Both examples
 500 confirm that the suction effect of the underlying subducting slabs on Earth

501 on upper plates is extremely efficient, in agreement with our models.

502 The topography in our models emerges from the stress balance and our scan-
503 ning device allows for a three-dimensional illustration of it. Four dimensional if
504 one accounts for its time evolution. The results often go beyond observational
505 possibilities, and as such they are potentially useful. These tests revealed that
506 analogue models are capable of predicting the evolution of the topography
507 around subduction zones. Specifically, they meet the following criteria: they
508 have free surfaces, they are three dimensional, subduction process is purely
509 dynamic (no kinematic boundary condition), rollback freely occurs. This del-
510 icate blend of conditions that are each individually still challenging to model
511 numerically makes our analogue models of use for the analysis and compre-
512 hension of the dynamics of relief. Last, these models give a simple view of the
513 three dimensional nature of the topography around subduction zones by com-
514 bining most processes that deform the surface of the Earth, but nevertheless
515 leave the possibility to extract each component independently, something that
516 is rendered difficult in real Earth, because of the uncertainty in the structure
517 of the lithosphere.

References

- [1] W. J. Morgan, Gravity Anomalies and Convection Currents, 1, A Sphere and Cylinder Sinking beneath the Surface of a Viscous Fluid, *Journal of Geophysical Research* 70 (1965) 6175–6187.
- [2] A. B. Watts, M. Talwani, Gravity Anomalies Seaward of Deep-Sea Trenches and their Tectonic Implications, *Geophysical Journal International* 36 (1974) 57–90.
- [3] H. J. Melosh, A. Raefsky, The dynamical origin of subduction zone topography, *Geophysical Journal* 60 (1980) 333–354.
- [4] S. Zhong, M. Gurnis, Viscous flow model of a subduction zone with a faulted lithosphere: Long and short wavelength topography, gravity and geoid, *Geophysical Research Letters* 19 (1992) 1891–1894.
- [5] L. Husson, Dynamic topography above retreating subduction zones, *Geology* 34 (2006) 741–+.
- [6] P. Colin, L. Fleitout, Topography of the ocean floor: Thermal evolution of the lithosphere and interaction of deep mantle heterogeneities with the lithosphere, *Geophysical Research Letters* 17 (1990) 1961–1964.
- [7] O. Čadež, L. Fleitout, Effect of lateral viscosity variations in the top 300 km on the geoid and dynamic topography, *Geophysical Journal International* 152 (2003) 566–580.
- [8] R. Moucha, A. M. Forte, J. X. Mitrovica, D. B. Rowley, S. Quéré, N. A. Simmons, S. P. Grand, Dynamic topography and long-term sea-level variations: There is no such thing as a stable continental platform, *Earth and Planetary Science Letters* 271 (2008) 101–108.
- [9] C. P. Conrad, L. Husson, Influence of dynamic topography on sea level and its rate of change, *Lithosphere* 1 (2) (2009) 110–120.
- [10] M. Gurnis, Ridge spreading, subduction, and sea level fluctuations, *Science* 250 (1990) 970–972.
- [11] M. Gurnis, Rapid Continental Subsidence Following the Initiation and Evolution of Subduction, *Science* 255 (1992) 1556–1558.
- [12] J. Mitrovica, The devonian to permian sedimentation of the Russian Platform: An example of subduction-controlled long-wavelength tilting of continents, *Journal of Geodynamics* 22 (1996) 79–96.
- [13] L. Liu, S. Spasojević, M. Gurnis, Reconstructing Farallon Plate Subduction Beneath North America Back to the Late Cretaceous, *Science* 322 (2008) 934–.
- [14] S. Spasojevic, L. Liu, M. Gurnis, Adjoint models of mantle convection with seismic, plate motion, and stratigraphic constraints: North America since the Late Cretaceous, *Geochemistry, Geophysics, Geosystems* 10 (2009) 5–+.

- [15] C. Faccenna, T. W. Becker, Shaping mobile belts by small-scale convection, *Nature* 465 (2010) 602–605.
- [16] L. Boschi, C. Faccenna, T. W. Becker, Mantle structure and dynamic topography in the Mediterranean Basin, *Geophys. Res. Lett.* 37 (2010) 20303–+.
- [17] Y. Krien, L. Fleitout, Gravity above subduction zones and forces controlling plate motions, *Journal of Geophysical Research (Solid Earth)* 113 (2008) 9407–+.
- [18] P. Wheeler, N. White, Quest for dynamic topography: Observations from Southeast Asia, *Geology* 28 (2000) 963–+.
- [19] M. I. Billen, M. Gurnis, Constraints on subducting plate strength within the Kermadec trench, *Journal of Geophysical Research (Solid Earth)* 110 (2005) 5407–+.
- [20] S. J. H. Buiter, R. Govers, M. J. R. Wortel, A modelling study of vertical surface displacements at convergent plate margins, *Geophysical Journal International* 147 (2001) 415–427.
- [21] M. I. Billen, M. Gurnis, M. Simons, Multiscale dynamics of the Tonga-Kermadec subduction zone, *Geophysical Journal International* 153 (2003) 359–388.
- [22] F. Funiciello, C. Faccenna, D. Giardini, K. Regenauer-Lieb, Dynamics of retreating slabs: 2. Insights from three-dimensional laboratory experiments, *Journal of Geophysical Research* 108 (2003) 2207–+.
- [23] W. P. Schellart, Kinematics of subduction and subduction-induced flow in the upper mantle, *Journal of Geophysical Research* 109 (2004) 7401–+.
- [24] N. Bellahsen, C. Faccenna, F. Funiciello, Dynamics of subduction and plate motion in laboratory experiments: Insights into the “plate tectonics” behavior of the Earth, *Journal of Geophysical Research (Solid Earth)* 110 (2005) 1401–+.
- [25] R. Weijermars, H. Schmeling, Scaling of Newtonian and non Newtonian fluid dynamics without inertia for quantitative modelling of rock flow due to gravity (including the concept of rheological similarity), *Physics of the Earth and Planetary Interiors* 43 (1986) 316–330.
- [26] P. Davy, P. R. Cobbold, Experiments of a 4-layered continental lithosphere, *Tectonophysics* 188 (1991) 1–25.
- [27] F. Funiciello, C. Faccenna, A. Heuret, S. Lallemand, E. di Giuseppe, T. W. Becker, Trench migration, net rotation and slab mantle coupling, *Earth and Planetary Science Letters* 271 (2008) 233–240.
- [28] W. P. Schellart, Kinematics and flow patterns in deep mantle and upper mantle subduction models: Influence of the mantle depth and slab to mantle viscosity ratio, *Geochemistry, Geophysics, Geosystems* 9 (2008) 3014–+.

- [29] B. Wu, C. P. Conrad, A. Heuret, C. Lithgow-Bertelloni, S. Lallemand, Reconciling strong slab pull and weak plate bending: The plate motion constraint on the strength of mantle slabs, *Earth and Planetary Science Letters* 272 (2008) 412–421.
- [30] C. Loiselet, L. Husson, J. Braun, From longitudinal slab curvature to slab rheology, *Geology* 37 (8) (2009) 747–750.
- [31] C. Kincaid, P. Olson, An experimental study of subduction and slab migration, *J. Geophys. Res.*92 (1987) 13832–13840.
- [32] W. P. Schellart, Evolution of the slab bending radius and the bending dissipation in three-dimensional subduction models with a variable slab to upper mantle viscosity ratio, *Earth and Planetary Science Letters* 288 (2009) 309–319.
- [33] G. Stadler, M. Gurnis, C. Burstedde, L. C. Wilcox, L. Alisic, O. Ghattas, The Dynamics of Plate Tectonics and Mantle Flow: From Local to Global Scales, *Science* 329 (2010) 1033–.
- [34] W. Jacoby, Paraffin model experiment of plate tectonics, *Tectonophysics* 35 (1976) 103–113.
- [35] N. M. Ribe, Bending mechanics and mode selection in free subduction: a thin-sheet analysis, *Geophysical Journal International* 180 (2010) 559–576.
- [36] B. Guillaume, J. Martinod, L. Husson, M. Roddaz, R. Riquelme, Neogene uplift of central eastern Patagonia: Dynamic response to active spreading ridge subduction?, *Tectonics* 28 (2009) C2009+.
- [37] P. Yamato, L. Husson, J. Braun, C. Loiselet, C. Thieulot, Influence of surrounding plates on 3D subduction dynamics, *Geophys. Res. Lett.*36 (2009) 7303–+.
- [38] F. A. Capitanio, D. R. Stegman, L. N. Moresi, W. Sharples, Upper plate controls on deep subduction, trench migrations and deformations at convergent margins, *Tectonophysics* 483 (2010) 80–92.
- [39] C. Piromallo, T. W. Becker, F. Funiciello, C. Faccenna, Three-dimensional instantaneous mantle flow induced by subduction, *Geophys. Res. Lett.*33 (2006) 8304–+.
- [40] F. Funiciello, M. Moroni, C. Piromallo, C. Faccenna, A. Cenedese, H. A. Bui, Mapping mantle flow during retreating subduction: Laboratory models analyzed by feature tracking, *Journal of Geophysical Research (Solid Earth)* 111 (2006) 3402–+.
- [41] S. Zhong, M. Gurnis, Controls on trench topography from dynamic models of subducted slabs, *J. Geophys. Res.*99 (1994) 15683–+.
- [42] J. G. Caldwell, W. F. Haxby, D. E. Karig, D. L. Turcotte, On the applicability of a universal elastic trench profile, *Earth and Planetary Science Letters* 31 (1976) 239–246.

- [43] J. De Bremaecker, Is the oceanic lithosphere elastic or viscous?, *Journal of Geophysical Research* 82 (1977) 2001–2004.
- [44] M. Gurnis, Plate-mantle coupling and continental flooding, *Geophysical Research Letters* 17 (1990) 623–626.
- [45] L. Husson, C. P. Conrad, Tectonic velocities, dynamic topography, and relative sea level, *Geophys. Res. Lett.* 33 (2006) 18303–+.
- [46] L. Husson, J. Brun, P. Yamato, C. Faccenna, Episodic slab rollback fosters exhumation of HP-UHP rocks, *Geophysical Journal International* 179 (2009) 1292–1300.
- [47] B. Parsons, P. Molnar, The Origin of Outer Topographic Rises Associated with Trenches, *Geophysical Journal International* 45 (1976) 707–712.
- [48] R. I. Walcott, Flexural Rigidity, Thickness, and Viscosity of the Lithosphere, *J. Geophys. Res.* 75 (1970) 3941–3954.
- [49] H. J. Melosh, Dynamic support of the outer rise, *Geophys. Res. Lett.* 5 (1978) 321–324.
- [50] T. Korenaga, J. Korenaga, Subsidence of normal oceanic lithosphere, apparent thermal expansivity, and seafloor flattening, *Earth and Planetary Science Letters* 268 (2008) 41–51.
- [51] R. M. Russo, P. G. Silver, Trench-Parallel Flow Beneath the Nazca Plate from Seismic Anisotropy, *Science* 263 (1994) 1105–1111.
- [52] F. M. Davila, C. Lithgow-Bertelloni, M. Gimenez, Tectonic and dynamic controls on the topography and subsidence of the Argentine Pampas: the role of the flat slab, *Earth and Planetary Science Letters* 295 (2010) 187–194.
- [53] J. Braun, The many surface expressions of mantle dynamics, *Nature Geoscience* 3 (12) (2010) 825–833.
- [54] R. D. Müller, M. Sdrolias, C. Gaina, W. R. Roest, Age, spreading rates, and spreading asymmetry of the world’s ocean crust, *Geochemistry, Geophysics, Geosystems* 9 (2008) 4006–+.

	Parameters		Nature	Reference model
g	Gravitational acceleration	m/s^2	9.81	9.81
<i>Length</i>				
W	Subducting plate width	m	990000	0.15
H	Subducting plate thickness		100000	0.0152
D	Upper mantle thickness		660000	0.10
	Scale factor for length		$L_{model}/L_{nature} = 1.52 \times 10^{-7}$	
<i>Buoyancy</i>				
$\rho_m - \rho_l$	Subducting oceanic plate	kg/m^3	-80	-91
			(80 Myr-old plate)	
	Scale factor for buoyancy		$\Delta\rho_{model}/\Delta\rho_{nature} \simeq 1$	
<i>Viscosity</i>				
η_l	Subducting oceanic plate	Pas	1.4×10^{24}	4.2×10^5
η_m	Upper mantle		10^{20}	30
	Scale factor for viscosity		$\eta_{model}/\eta_{nature} = 3 \times 10^{-19}$	
<i>Characteristic time</i>				
t	$t_{nature}/t_{model} = ((\Delta\rho g H)_{model}/(\Delta\rho g H)_{nature}) \times (\eta_{nature}/\eta_{model})$	s	3.16×10^{13} (1 Myr)	55
	Scale factor for time		$t_{model}/t_{nature} = 1.74 \times 10^{-12}$	

Table 1
Scaling of the modeling parameters in nature and in the laboratory, for the reference model.

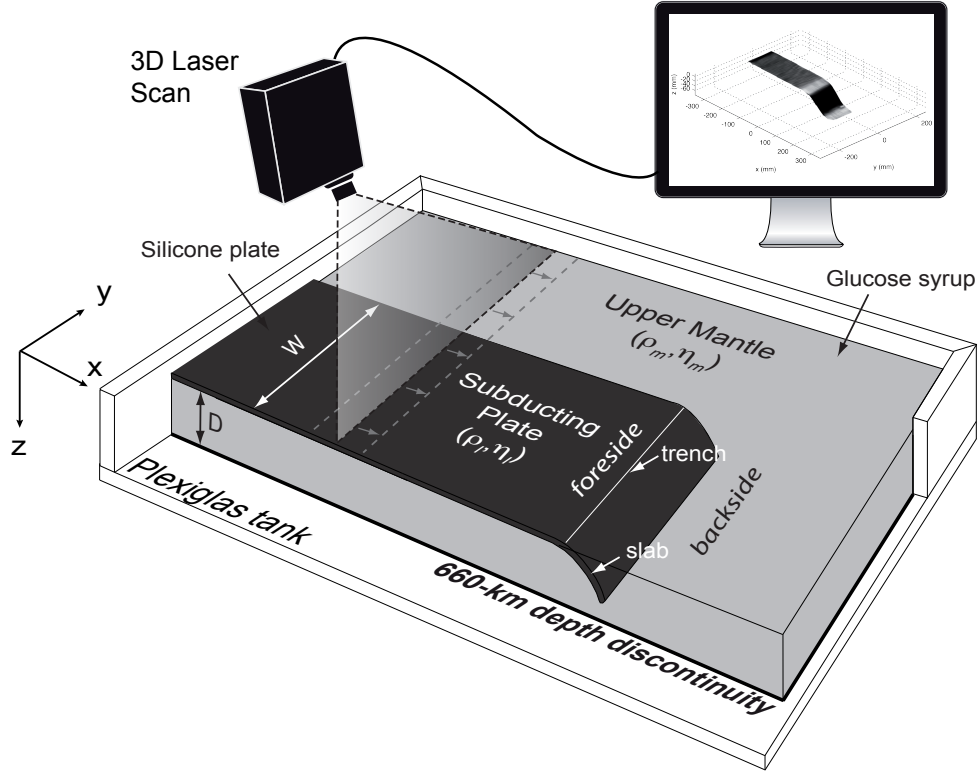


Fig. 1. Experimental setup. The subducting lithosphere is modeled by a silicone plate of density ρ_l , viscosity η_l , width W , thickness H . The mantle is simulated by means of glucose syrup of density ρ_m , viscosity η_m and thickness D . The plate is either *fixed*, *i.e.* the trailing edge is attached to the end of the tanks or *free*, *i.e.* the trailing edge freely moves. The surface topography in the experiments is monitored by a 3D laser scanner. The foreside corresponds to the region where the lithosphere has not yet been subducted and the backside is located above the sunken slab.

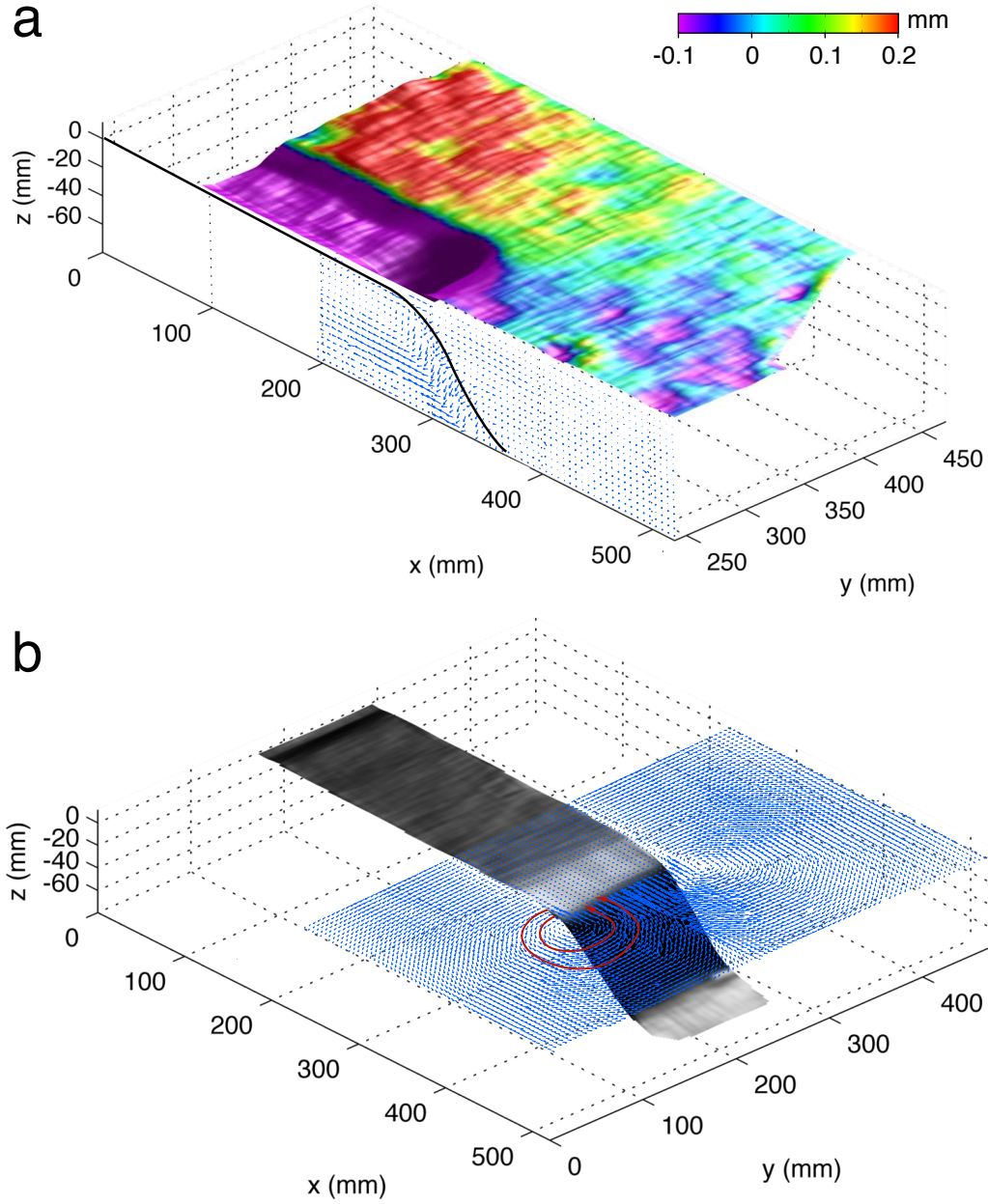


Fig. 2. (a) 3D view of the surface topography (color coded and magnified by a factor 10) cut along the plate centerline and velocity vectors (in blue) of the mantle flow in the vertical section (x - z) for our reference experiment with *fixed edge* conditions (model 1, see parameters in Table 1). (b) 3D view of the top of the slab shape (in black) and velocity vectors (in blue) of the mantle flow in the horizontal section (x - y) at the top of the mantle for the same model.

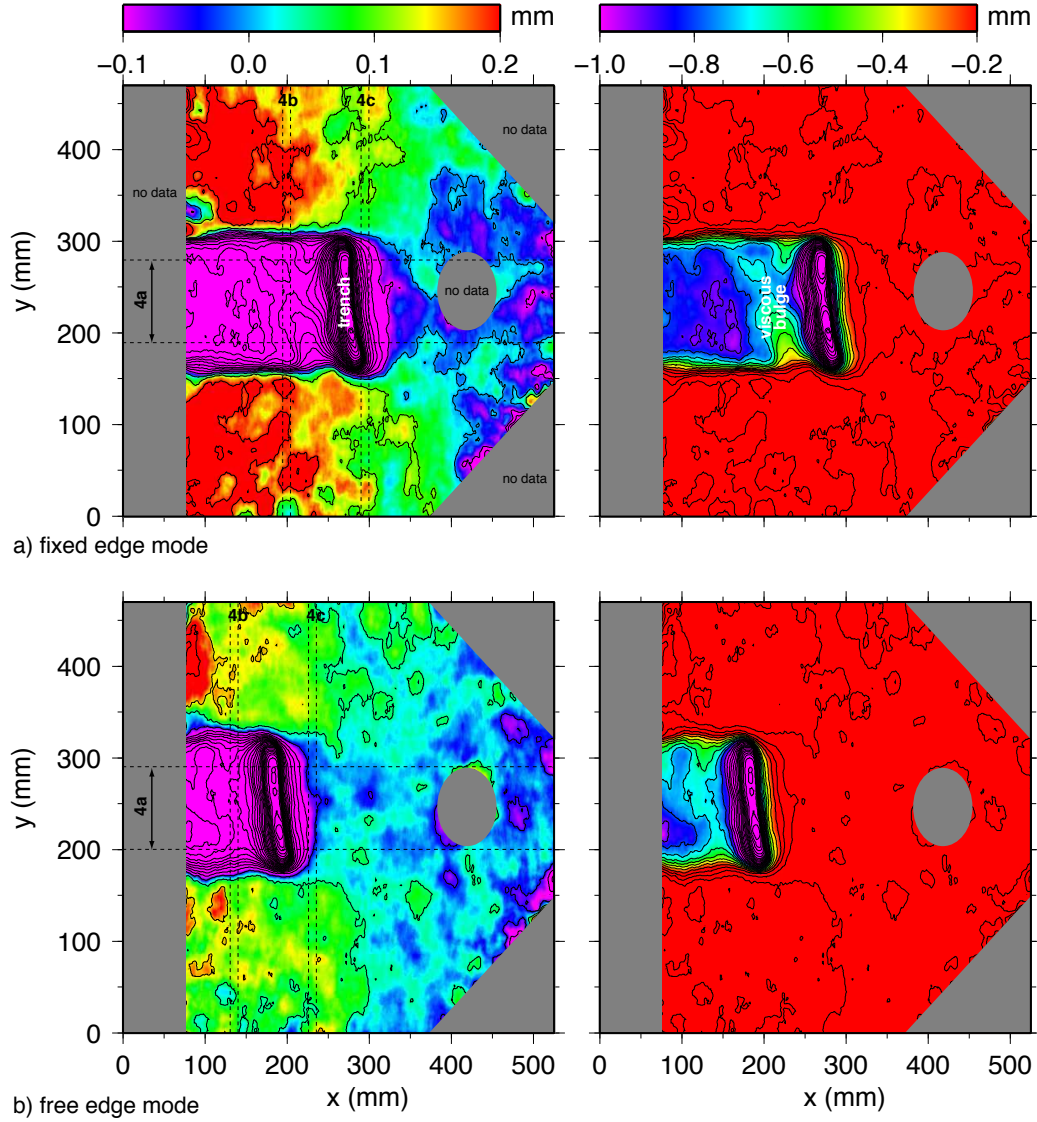


Fig. 3. Map view of the surface of model 1 in the *fixed* (a) and *free* (b) subduction modes. Right and left panels display the same maps but with different color palettes in order to respectively highlight the topography of the plate (right) and glucose syrup (left). The dotted lines show the location of the different swath profiles plotted in fig. 4. Areas with no topographic data are indicated in gray.

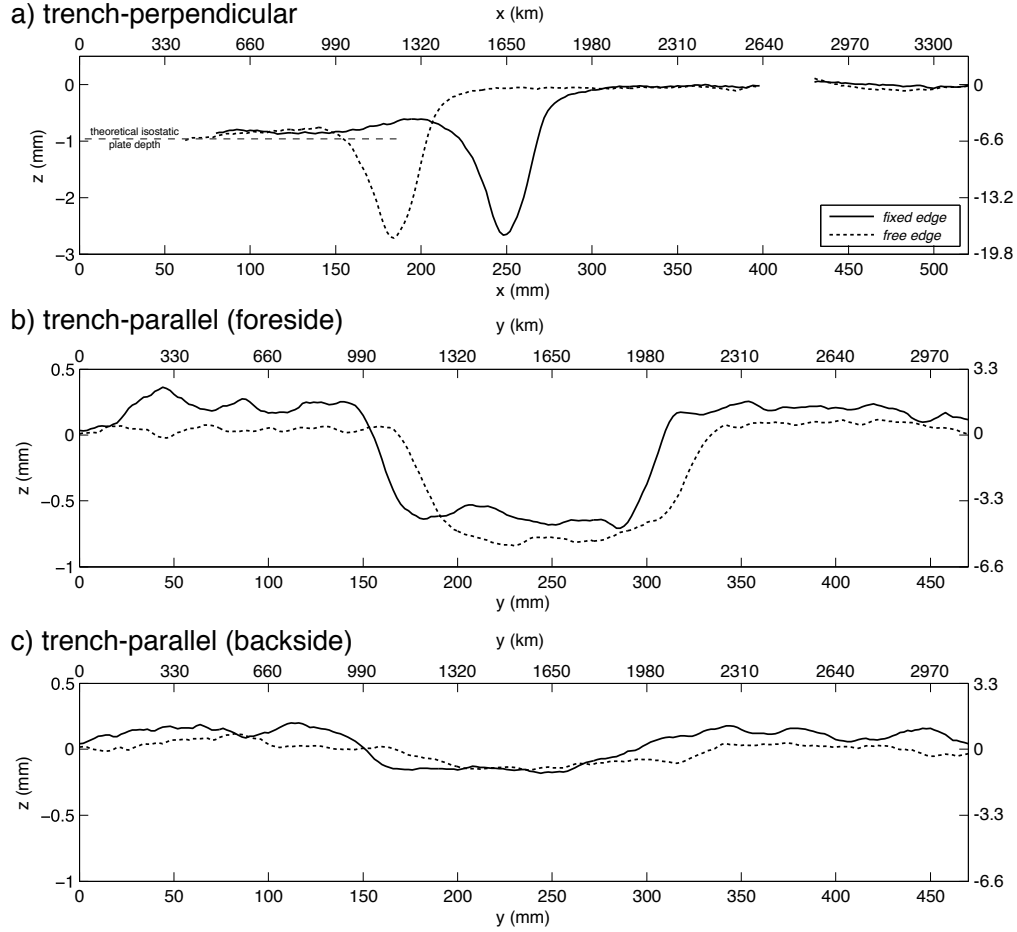


Fig. 4. Swath topographic profiles for model 1 in the *fixed* (solid line) and *free* (dotted line) subduction modes (a) in the trench-normal direction, averaged over a distance of 40 mm from the plate centerline, (b) in the trench-parallel direction in the foreside (50 mm from the trench), and (c) in the trench-parallel direction in the backside (50 mm from the trench). Note the different scales for fig. 4a and figs. 4b-c. See fig. 3 for sections location. The theoretical isostatic depth for the plate is indicated by a dashed line in the first panel.

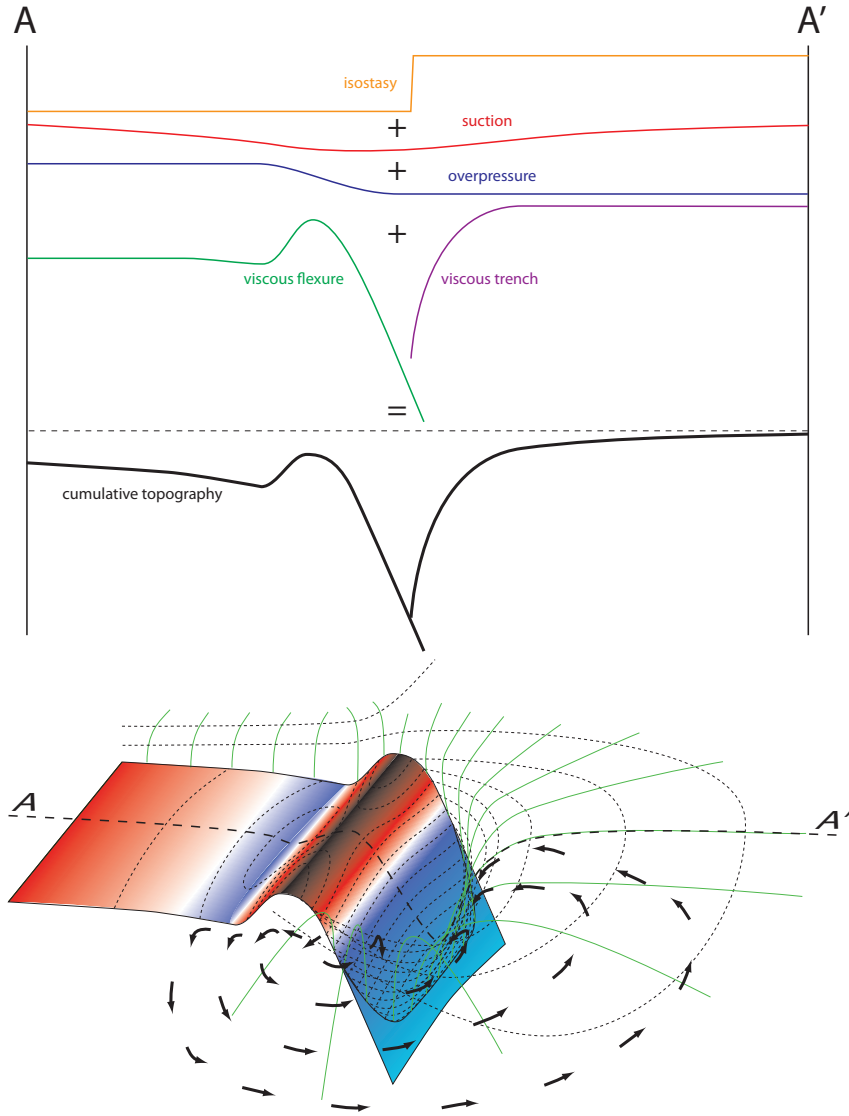


Fig. 5. Synthetic 3D sketch of the topography around a subduction zone (bottom) in the experiments (not to scale). Black dotted lines are isodepths curves, green curves follow the local maximum topographic gradients. Black arrows denote the flow pattern from below the slab on the foreside to above the slab on the backside. Top graph shows the isolated contributors along the central cross-section AA' .

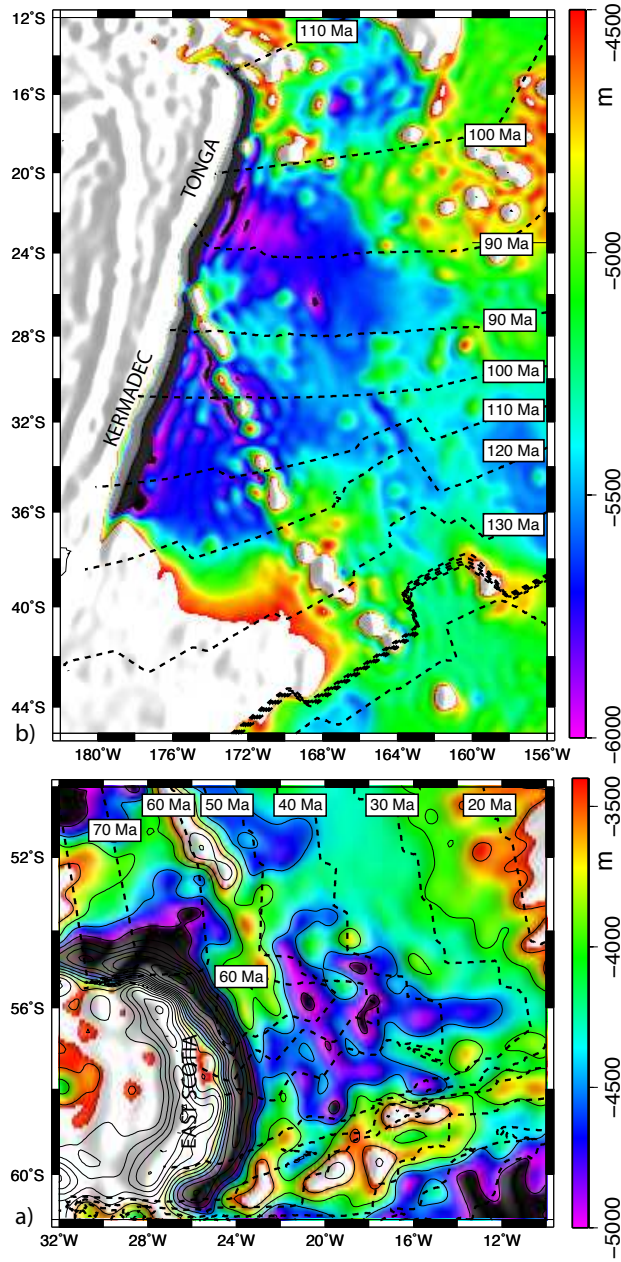


Fig. 6. Bathymetry on the foresides of the East Scotia (a) and Tonga and Kermadec (b) subduction zones. Wavelengths shorter than 100 km have been filtered out. Note the low lying areas on the foresides of each trench, ~ 5000 m deep (East Scotia), ~ 6000 m deep (Tonga) and ~ 5700 m deep (Kermadec). In all three cases, they are 800 to 1000 m deeper than the adjacent seafloor of similar age. Seafloor age from [54].

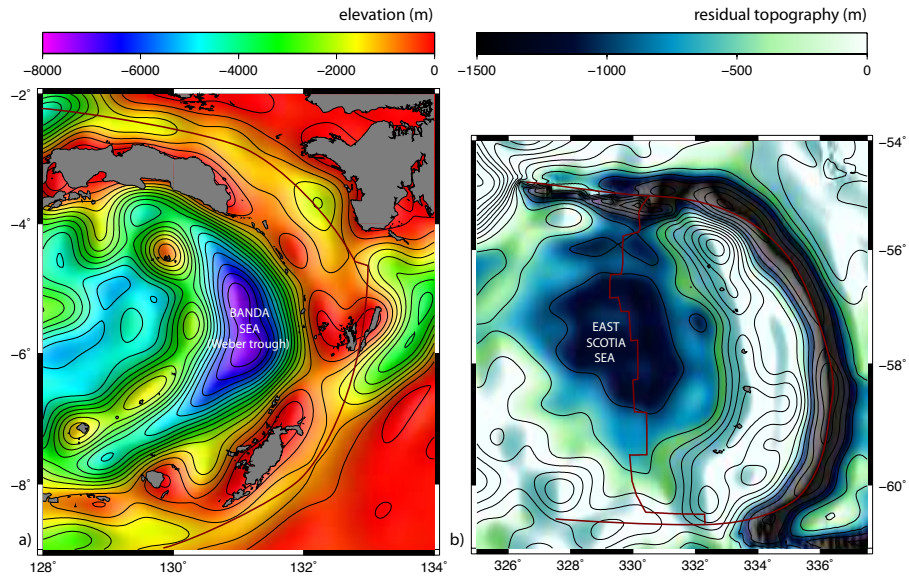


Fig. 7. Bathymetry on the backside of the Banda subduction zone (a) and residual bathymetry of the East Scotia subduction zone (b, modified after [5]). (Residual topography of the extremely young Banda back-arc basin was not computed (unavailable seafloor age grid) but is expected to be almost comparable to the residual topography). Wavelengths shorter than 100 km have been filtered out. Note the ~ 8000 m deep Weber trough on the backside of Banda trench, and the ~ 1500 m residual topography in the East Scotia back arc basin.

Supplementary material 1.

Experimental parameters. (W : plate width; H : plate thickness; D : mantle thickness ρ_l : plate density; η_l : plate viscosity; ρ_m : mantle density; η_m : mantle viscosity; ρ_{ll} : light plate density).

Model	W <i>mm</i>	H <i>mm</i>	D <i>mm</i>	ρ_l <i>kg/m³</i>	η_l <i>Pa s</i>	ρ_m <i>kg/m³</i>	η_m <i>Pa s</i>	ρ_{ll} <i>kg/m³</i>	η_l/η_m	$\rho_l - \rho_m$ <i>kg/m³</i>
1	150	15.2	100	1506	4.2×10^5	1415	30	-	14000	91
2	200	13.7	100	1468	3.0×10^5	1415	30	-	10000	53
3	150	12.5	100	1468	3.0×10^5	1415	30	-	10000	53
4	200	13.0	100	1506	4.2×10^5	1415	30	-	14000	91
5	200	15.5	100	1506	4.2×10^5	1415	30	-	14000	91
6	150	13.7	100	1506	4.2×10^5	1415	30	-	14000	91
7	145	15.5	100	1468	3.0×10^5	1415	30	-	10000	53
8	150	15.0	97	1506	4.2×10^5	1450	1000	-	420	56
9	200	15.0	100	1506	4.2×10^5	1450	1000	-	420	56
10	200	12.8	98	1506	4.2×10^5	1450	1000	-	420	56
11	150	13.0	95	1506	4.2×10^5	1450	1000	-	420	56
12	150	12.0	100	1506	4.2×10^5	1450	1000	1458	420	56
13	150	12.0	100	1506	4.2×10^5	1450	1000	1458	420	56